Long-time behavior of three-dimensional gravity-capillary solitary waves on deep water generated by a moving air-blowing forcing: Numerical study

Yeunwoo Cho[*]

Department of Mechanical Engineering, Korea Advanced Institute of Science and Technology,
291 Daehak-ro, Yuseong-gu, Daejeon, 34141, Republic of Korea

Long-time simulations are conducted on a forced three-dimensional (3D) nonlinear viscous gravity-capillary wave equation that describes the surface wave pattern when the forcing moves on the surface of deep water with speeds less than the linear phase speed $c_{min} = 23$ cm/s. Three different states are identified according to forcing speeds U below c_{min}. At relatively low speeds below a certain speed (c_1), a steady circular dimple is observed below the moving forcing. At relatively high speeds above a certain speed (c_2), "symmetric" shedding phenomena of 3D depressions are observed behind the moving forcing. At intermediate speeds ($c_1 \leqslant U \leqslant c_2$), steady 3D gravity-capillary solitary waves are generated behind the moving forcing and are maintained for some time. After long-time simulations, however, those gravity-capillary solitary waves break up and 3D local depressions are shed asymmetrically behind the moving forcing. In more detail, when the forcing speed (U) is very close to c_1, the asymmetric shedding is "almost regular" and when the forcing speed (U) is very close to c_2, the asymmetric shedding is "regular antisymmetric," after a transient period of an "irregular" asymmetric shedding from the steady state of 3D gravity-capillary solitary waves. On the contrary, for the remaining cases of the entire forcing speeds ($c_1 < U < c_2$), the asymmetric shedding is "irregular."

I. INTRODUCTION

On deep water, the linear phase speed of a gravity-capillary wave features a minimum $c_{min} = 23$ cm/s at a nonzero wavelength $\lambda_{min} = 1.71$ cm. Below the minimum phase speed c_{min}, two-dimensional (2D) or three-dimensional (3D) gravity-capillary solitary waves of depression types can theoretically exist [1–11]. At low speeds below c_{min}, they are fully localized disturbances with finite-amplitude depressions. At speeds close to c_{min}, they are wavepacket-type disturbances with small-amplitude depressions. 2D gravity-capillary solitary waves are stable to longitudinal perturbations [12–14]. However, when subject to transverse perturbations, they are unstable and will eventually be transformed into finite-amplitude 3D gravity-capillary solitary waves [13–19]. Compared to their 2D counterparts, 3D gravity-capillary solitary waves have different stability characteristics. While finite-amplitude 3D gravity-capillary solitary waves are stable to longitudinal perturbations, small-amplitude 3D gravity-capillary solitary waves of wavepacket types are unstable to longitudinal perturbations [13,17,20,21]. Therefore, only finite-amplitude 3D gravity-capillary solitary waves are expected to be physically relevant and they really were observed in the experiments. The first observation of finite-amplitude 3D gravity-capillary solitary waves, although not definitive, was made by Zhang [22] in a wind-wave experiment. Recently, more definitive observations of finite-amplitude 3D gravity-capillary solitary waves were made from the experiments using a moving 3D air-blowing forcing [23–27] or a moving 3D air-suction forc-

ing [28]. In the works using 3D air-blowing forcings [23–25], three different states are identified according to forcing speeds U below c_{min}. At relatively low speeds below a certain speed $c_1(U < c_1)$, a steady circular dimple is observed below the moving forcing (termed as "state I" in Refs. [23–25]). At relatively high speeds above a certain speed $c_2(c_2 < U < c_{min})$, symmetric shedding phenomena of 3D depressions are observed behind the moving forcing (termed as "state III" in [23–25]). At intermediate speeds ($c_1 \leqslant U \leqslant c_2$), steady 3D gravity-capillary solitary waves are generated behind the moving forcing (termed as "state II" in Refs. [23–25]). In all these works, however, observations of long-time behaviors of forced 3D gravity-capillary solitary waves were not made mainly due to the spatial limitation, i.e., finite length of the wave tank which is short for a long-time experiment. Therefore, this became the subject of the present numerical work, where the focus is put on the long-time behavior of forced finite-amplitude 3D gravity-capillary solitary waves on deep water generated by a moving air-blowing forcing. Relevant numerical simulation was recently performed in the work of Masnadi and Duncan [26] using a model equation described in Ref. [25]. By solving this model equation numerically, for some early time (a few seconds), they observed a stable configuration where steady forced 3D gravity-capillary solitary waves are formed behind the moving air-blowing forcing. After a longer-time simulation, however, this configuration becomes unstable and an irregular asymmetric shedding of 3D local depressions behind the moving forcing are identified. No direct comparison of this numerical result with a corresponding experiment is made due to the finite length of the wave tank which is short for a long-time experiment. Instead, during a relatively short time, they experimentally observed an

―――――――
[*]ywoocho@kaist.ac.kr

irregular asymmetric shedding of 3D local depressions behind the moving forcing, when the forcing speed is within the sharp boundary between two different states, state II and state III (termed in Refs. [23–25]). Motivated by their works, in the present paper, more definitive numerical results are reported to investigate the long-time irregular asymmetric shedding behavior of forced finite-amplitude 3D gravity-capillary solitary waves for the speed range, $c_1 < U < c_2$ (termed as "state II" in Refs. [23–25]). Furthermore, when the forcing speed (U) is very close to c_1, the present numerical simulation will show that the "almost regular" shedding is finally observed after a transient period of an "irregular" asymmetric shedding from the steady state of 3D gravity-capillary solitary waves. Similarly, when the forcing speed (U) is very close to c_2, the present numerical simulation will show that the "regular antisymmetric" shedding is finally observed after a transient period of an "irregular" asymmetric shedding from the steady state of 3D gravity-capillary solitary waves.

In Sec. II, the adopted numerical method is described to solve a model equation of forced 3D gravity-capillary solitary waves on deep water [25]. In Sec. III, numerical results of long-time simulations of the model equation are presented according to various forcing speeds. In Sec. IV, the asymmetric shedding is analyzed based on the linear stability analysis. Finally, Sec. V is the summary.

II. NUMERICAL METHOD

In the frame of reference moving left with a dimensionless forcing speed α ($= U/c_{\min}$, where U is a

dimensional forcing speed), the dimensionless theoretical model equation in terms of dimensionless wave elevation (η) for forced finite-amplitude 3D gravity-capillary solitary waves on deep water under the influence of viscosity is as follows [16,25,28]:

$$\underbrace{\eta_t + \alpha \eta_x}_{\text{Convection}} \underbrace{-\tilde{\nu}(\eta_{xx} + \eta_{yy})}_{\text{Viscous dissipation}} \underbrace{-\frac{1}{2}\eta_x - \frac{1}{4}\mathcal{H}\{\eta_{xx} + 2\eta_{yy} - \eta\}}_{\text{Dispersion}}$$

$$\underbrace{-\beta(\eta^2)_x}_{\text{Nonlinear steepening}} = \underbrace{A p_x}_{\text{Forcing}} . \quad (1)$$

The derivation of the dimensionless equation Eq. (1) starts from the dimensionless dispersion relation of gravity-capillary waves on deep water based on the characteristic length $L = (\sigma/\rho g)^{1/2}$ and the characteristic time $T = \sigma^{1/4}/(2^{1/2}\rho^{1/4}g^{3/4})$. The detailed derivation is given in Appendix. In Eq. (1), the dimensionless viscosity is $\tilde{\nu} = C\nu(4g)^{1/4}(\rho/\sigma)^{3/4} = 0.003C$ ($\nu = 10^{-6}$ m^2/s, $g = 9.81$ m/s^2, $\rho = 1000$ kg/m^3, $\sigma = 0.073$ N/m), the dimensionless coefficient of the quadratic nonlinearity is $\beta = \sqrt{11/2}/8$, the dimensionless forcing magnitude is $A = 0.23$ and the dimensionless forcing function is $p(x, y) = \exp(-2x^2 - 2y^2)$, whose shape is hinted from the relevant experiments [24,25]. The operator H is the Hilbert transform and the parameter C is set to be 2.4 such that numerical results best fit experimental results [24,25]. If one wishes to obtain the dimensional version of Eq. (1), $t = t'/T$, $x = x'/L$, $y = y'/L$, and $\eta = \eta'/L$ (primed variables denote dimensional ones) can be substituted in Eq. (1) as follows:

$$\underbrace{\eta'_{t'} + \frac{L}{T}\alpha \eta'_{x'}}_{\text{Convection}} \underbrace{-\frac{L^2}{T}\tilde{\nu}(\eta'_{x'x'} + \eta'_{y'y'})}_{\text{Viscous dissipation}} \underbrace{-\frac{L}{2T}\eta'_{x'} - \frac{L^2}{4T}\mathcal{H}\left\{\eta'_{x'x'} + 2\eta'_{y'y'} - \frac{1}{L^2}\eta'\right\}}_{\text{Dispersion}} \underbrace{-\frac{\beta}{T}(\eta'^2)_{x'}}_{\text{Nonlinear steepenging}} = \underbrace{\frac{L^2 A}{T}p_{x'}}_{\text{Forcing}} . \quad (2)$$

For numerical computations, by taking the spatial Fourier transform of Eq. (1),

$$\hat{\eta}_t = \left\{-\tilde{\nu}(k^2 + l^2) - ik\left(\alpha - \tfrac{1}{2}\right) + \tfrac{1}{4}i\,\text{sgn}(k)(k^2 + 2l^2 + 1)\right\}\hat{\eta}$$
$$+ \beta ik FT\{\eta^2\} + Aik\hat{p}, \quad (3)$$

$$FT\{\eta\} = \hat{\eta}(k, l, t) = \int_{-\infty}^{\infty}\int_{-\infty}^{\infty}\eta(x, y, t)e^{-ikx-ily}dx dy, \quad (4)$$

$$FT\{p\} = \hat{p}(k, l) = \int_{-\infty}^{\infty}\int_{-\infty}^{\infty}p(x, y)e^{-ikx-ily}dx dy, \quad (5)$$

$$\eta(x, y, t) = FT^{-1}\{\hat{\eta}(k, l, t)\}$$
$$= \frac{1}{2\pi}\int_{-\infty}^{\infty}\int_{-\infty}^{\infty}\hat{\eta}(k, l, t)e^{ikx+ily}dk dl, \quad (6)$$

$$FT\{\eta^2\} = FT\{(FT^{-1}\{\hat{\eta}\})^2\}. \quad (7)$$

In the real computation of the Fourier and inverse Fourier transforms, at each time step, for input data $\mathbf{x}(n_1, n_2)$

($n_1 = 1, 2, \cdots, M$, $n_2 = 1, 2, \cdots, N$) and $\mathbf{X}(r_1, r_2)$ ($r_1 = 1, 2, \cdots, M, r_2 = 1, 2, \cdots, N$), following FFT (fast Fourier transform) pairs are used:

$$FT\{\mathbf{x}(n_1, n_2)\} = \sum_{n_1=1}^{M}\sum_{n_2=1}^{N}\mathbf{x}(n_1, n_2)$$
$$\times e^{-j\frac{2\pi}{M}(r_1-1)(n_1-1)}e^{-j\frac{2\pi}{N}(r_2-1)(n_2-1)}$$
$$= \mathbf{X}(r_1, r_2), \quad (8)$$

$$FT^{-1}\{\mathbf{X}(r_1, r_2)\} = \frac{1}{MN}\sum_{r_1=1}^{M}\sum_{r_2=1}^{N}\mathbf{X}(r_1, r_2)e^{j\frac{2\pi}{M}(r_1-1)(n_1-1)}$$
$$\times e^{j\frac{2\pi}{N}(r_2-1)(n_2-1)}$$
$$= \mathbf{x}(n_1, n_2), \quad (9)$$

where j is the complex number satisfying $j^2 = -1$. Equation (3) is the first-order ordinary differential equation in terms of
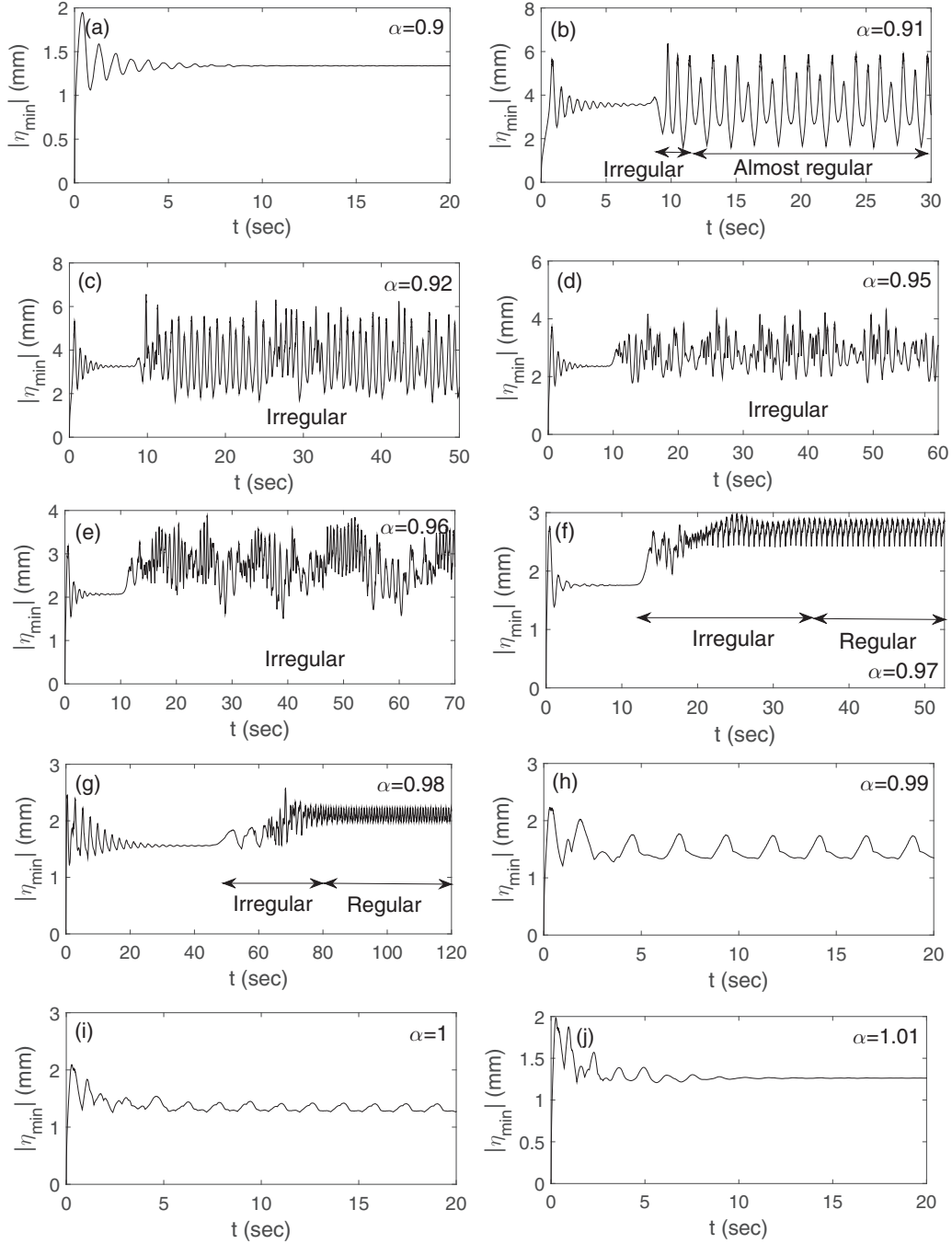
FIG. 1. Time histories of the maximum depressions of the solutions to Eq. (1) with the initial still-water condition according to forcing speeds α.

time and can be written in the following canonical form:

$$\hat{\eta}_t \equiv F(\hat{\eta}). \tag{10}$$

Equation (10) is solved using the explicit Euler time stepping combined with the predictor-corrector scheme as follows:

$$\hat{\eta}_p^{(i+1)} = \hat{\eta}^{(i)} + \Delta t \, F(\hat{\eta}^{(i)}) \quad \text{(Predictor)}, \tag{11}$$

$$\hat{\eta}^{(i+1)} = \hat{\eta}^{(i)} + \frac{\Delta t}{2}\left\{F\left(\hat{\eta}_p^{(i+1)}\right) + F\left(\hat{\eta}^{(i)}\right)\right\} \quad \text{(Corrector)}, \tag{12}$$

where the superscript denotes the discrete time.

III. NUMERICAL RESULTS

In the numerical simulations, the time step $\Delta t = 0.001$ and spatial resolutions of $\Delta x = 0.15$, $\Delta y = 0.3$ in the domain $-12\pi < x < 12\pi$, $-12\pi < y < 12\pi$ ($M = 512$, $N = 256$) are used for a stable computation for a long time ($\sim t = 800$). The initial condition is a still-water condition (zero everywhere). The boundary conditions are periodic boundary conditions in both x and y directions. If the domain size is not large enough, disturbances propagating toward one boundary will come out from the opposite boundary due to the periodic boundary conditions. To minimize this, a sufficiently large domain size ($-12\pi < x < 12\pi$, $-12\pi < y < 12\pi$) is used

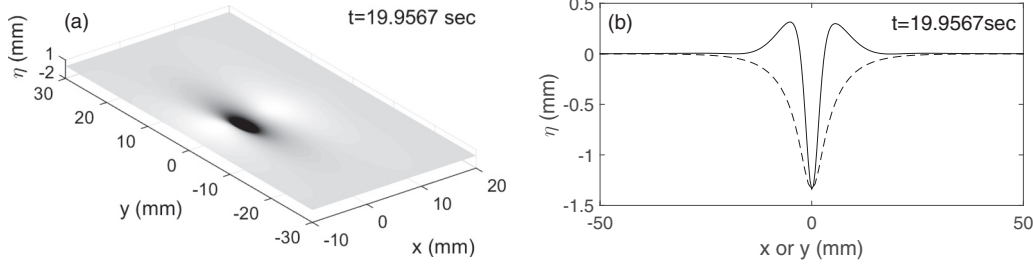FIG. 2. Steady wave solution corresponding to Fig. 1(a) ($\alpha = 0.9$). The left moving forcing is located at the origin ($x = 0$, $y = 0$). A steady dimple is formed just below the moving forcing. (a) Slanted view, (b) Cross-sectional view (solid line: profile on the $y = 0$ plane, dashed line: profile on the plane which passes through the minimum of the profile on the $y = 0$ plane).

such that disturbances propagating towards one boundary can have enough time to be dissipated due to the viscosity before the arrival at the boundary. For dimensional results, the characteristic length $L = (\sigma/\rho g)^{1/2} = 2.73$ mm and the characteristic time $T = L/c_{\min} = \sigma^{1/4}/(2^{1/2}\rho^{1/4}g^{3/4}) = 0.0118$ s are multiplied to dimensionless results. Figure 1 shows the time history of the maximum depression of the wave solution to Eq. (1) according to forcing speeds $0.9 \leqslant \alpha = U/c_{\min} \leqslant 1.01$. In the large, there are four different types of wave solutions (three different types of wave solutions below $\alpha = 1$). First, when $\alpha \leqslant 0.9$ [Fig. 1(a)], the wave solution is the steady dimple just below the moving forcing as shown in Fig. 2 ($\alpha = 0.9$). As the forcing speed increases ($0.91 \leqslant \alpha \leqslant 0.98$) as in Figs. 1(b)–1(g), steady 3D gravity-capillary solitary waves are generated behind the moving forcing for some time. These steady wave solutions can actually be predicted by solving the following equation by ignoring the time dependent term in Eq. (1) as follows:

$$\alpha\eta_x - \tilde{\nu}(\eta_{xx} + \eta_{yy}) - \frac{1}{2}\eta_x - \beta(\eta^2)_x$$
$$- \frac{1}{4}\mathcal{H}\{\eta_{xx} + 2\eta_{yy} - \eta\} = Ap_x. \quad (13)$$

The adopted numerical method is the pseudoarclength continuation method [29]. Since Eq. (13) is a nonlinear PDE, multiple solutions can exist for a certain value of α. To find multiples solutions for η, the dimensionless forcing speed α is treated as an unknown rather than as a known fixed parameter. To find these two unknowns (α, η), the following two equations are considered:

$$G(\alpha, \eta) = \alpha\eta_x - \tilde{\nu}(\eta_{xx} + \eta_{yy}) - \frac{1}{2}\eta_x - \beta(\eta^2)_x$$
$$- \frac{1}{4}\mathcal{H}\{\eta_{xx} + 2\eta_{yy} - \eta\} - Ap_x = 0, \quad (14)$$

$$F(\alpha, \eta) = \mathbf{s}^T(\eta - \eta_0) + \sigma(\alpha - \alpha_0) - \Delta S = 0. \quad (15)$$

Equation (15) is the equation of the plane perpendicular to $\hat{\mathbf{t}} = (\sigma, \mathbf{s})$ at a distance ΔS from (α_0, η_0), where $\hat{\mathbf{t}} = (\sigma, \mathbf{s})$ is a unit-length psuedoarc or tangent at (α_0, η_0) on the solution branch and ΔS is the pseudoarclength. The discretized simultaneous system Eqs. (14) and (15) are solved using the Newton's method. For interested readers, more details can be found in Ref. [29]. Figures 3(a) and 3(b) show the resultant diagram between $|\eta_{\min}|$ and α, on which the steady solutions in Figs. 1(a)–1(g) are marked [Figs. 3(c)–3(h)]. Although the nonlinear solitary-wave solutions are found from the steady

equation, Eq. (13), they, however, are only temporarily steady in the long-time simulation of the unsteady equation, Eq. (1), as shown in Figs. 1(b)–1(g). The duration times of steady 3D gravity-capillary solitary waves increase as the forcing speeds α increase; about 3, 3, 4, 5, 8, 13s for $\alpha = 0.91$, 0.92, 0.95, 0.96, 0.97, 0.98, respectively. After long-time simulations, however, those gravity-capillary solitary waves break up and 3D local depressions are shed asymmetrically behind the moving forcing. In more detail, for the forcing speeds ($0.92 \leqslant \alpha \leqslant 0.96$), the asymmetric shedding is irregular [Figs. 1(c)–1(e)]. On the contrary, when the forcing speed (α) is very close to 0.9, the asymmetric shedding is "almost regular" after a transient period of an "irregular" asymmetric shedding from the steady state of 3D gravity-capillary solitary waves [Fig. 1(b)]. When the forcing speed (α) is very close to 0.99, the asymmetric shedding is "regular antisymmetric" after a transient period of an "irregular" asymmetric shedding from the steady state of 3D gravity-capillary solitary waves [Figs. 1(f) and 1(g)]. For example, for the forcing speed $\alpha = 0.97$, Fig. 1(f) shows the time history of the maximum depression of the solution to Eq. (1). After the first transient period ($\sim$4 s), the solution approaches a steady 3D gravity-capillary solitary wave solution (Fig. 4). This solitary wave solution maintains its stability for some time (4 $\sim$ 13 s), after which an "irregular" asymmetric shedding of 3D local depressions occurs during the second transient period (13 $\sim$ 35 s) (Fig. 5). Although the alternate left- and right-shedding can be seen, this shedding is irregular in that there is no period which can be clearly defined as shown in Fig. 1(f). As mentioned in the Introduction, this state is probably the one observed by Masnadi and Duncan [26]. Finally, after the second transient period, the final state becomes a "regular antisymmetric" shedding of 3D local depressions (Fig. 6). In Fig. 6(a), one can see the obliquely shed 3D local depression on the left side of the left-moving forcing. At the same time, near the forcing position, the growth of a new 3D local depression is seen which is going to be obliquely shed on the right side of the left-moving forcing. Then, as shown in Figs. 6(b) and 6(c), the left-side 3D local depression gradually disappears due to viscous dissipation while the new 3D local depression is being obliquely shed on the right side of the left-moving forcing under the influence of viscous dissipation. The same dissipation-growth phenomena are repeated for the shed and the newly growing 3D local depressions; Figs. 6(a)–6(d) are the same as Figs. 6(e)–6(h), respectively, and the
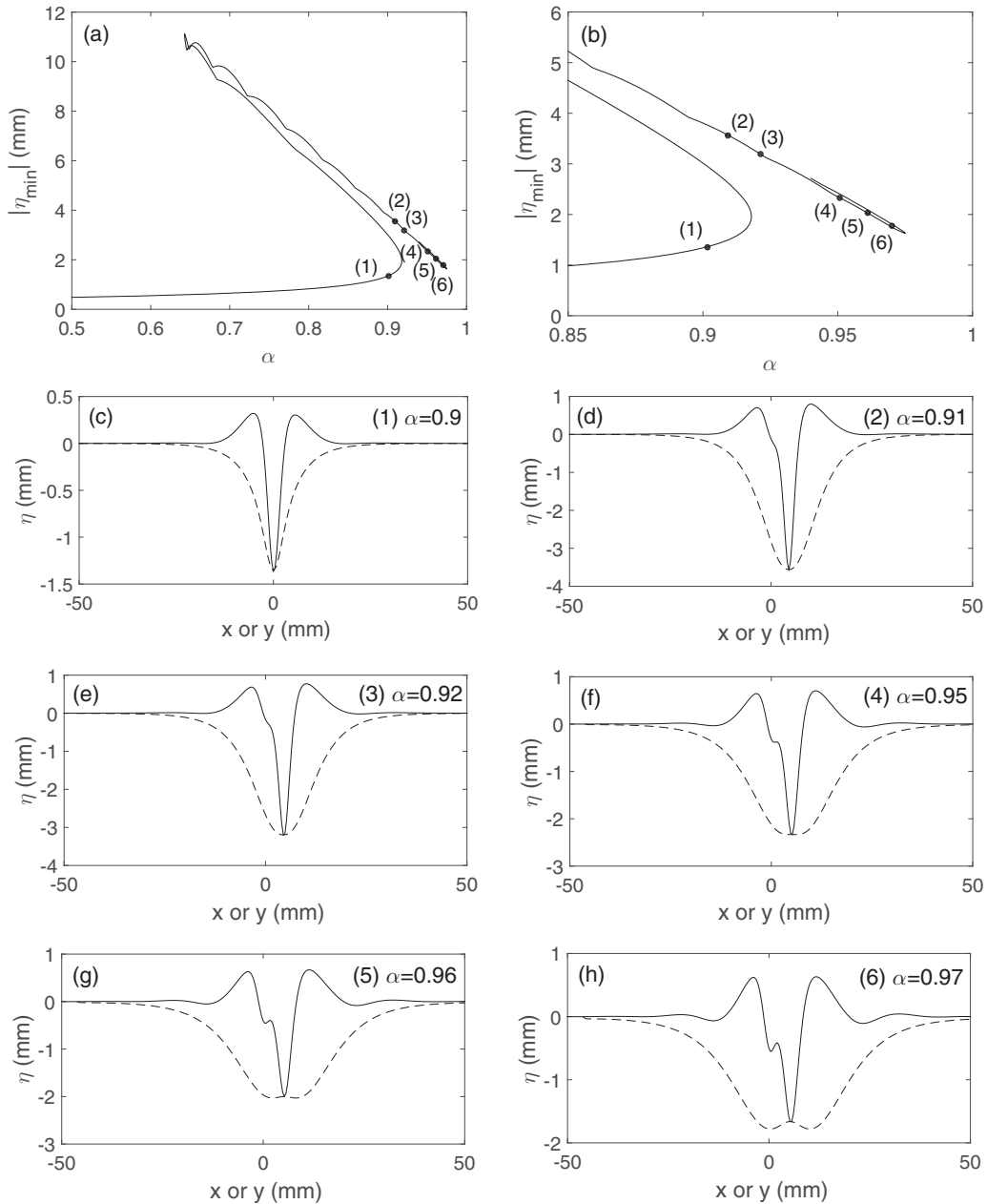
FIG. 3. Steady wave solutions from Eq. (13). (a) $|\eta_{min}|$ vs α diagram, (b) magnified version of Fig. 3(a) near $\alpha = 1$. (c)–(h) Cross-sectional view (solid line: profile on the $y = 0$ plane, dashed line: profile on the plane which passes through the minimum of the profile on the $y = 0$ plane) of steady solitary-wave solutions for $\alpha = 0.9, 0.91, 0.92, 0.95, 0.96,$ and 0.97 corresponding to the dot points (1)–(6) in (a) and (b). These solutions are the same as steady wave solutions in Figs. 1(b)–1(g).
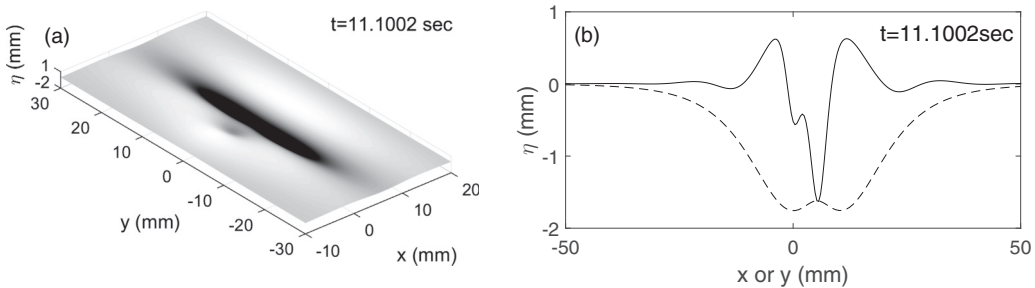

FIG. 4. Steady wave solution corresponding to Fig. 1(f) ($\alpha = 0.97$, $t = 4 \sim 13$ s). The left moving forcing is located at the origin ($x = 0$, $y = 0$). Steady solitary waves are formed behind the moving forcing. (a) Slanted view, (b) cross-sectional view (solid line: profile on the $y = 0$ plane, dashed line: profile on the plane which passes through the minimum of the profile on the $y = 0$ plane).
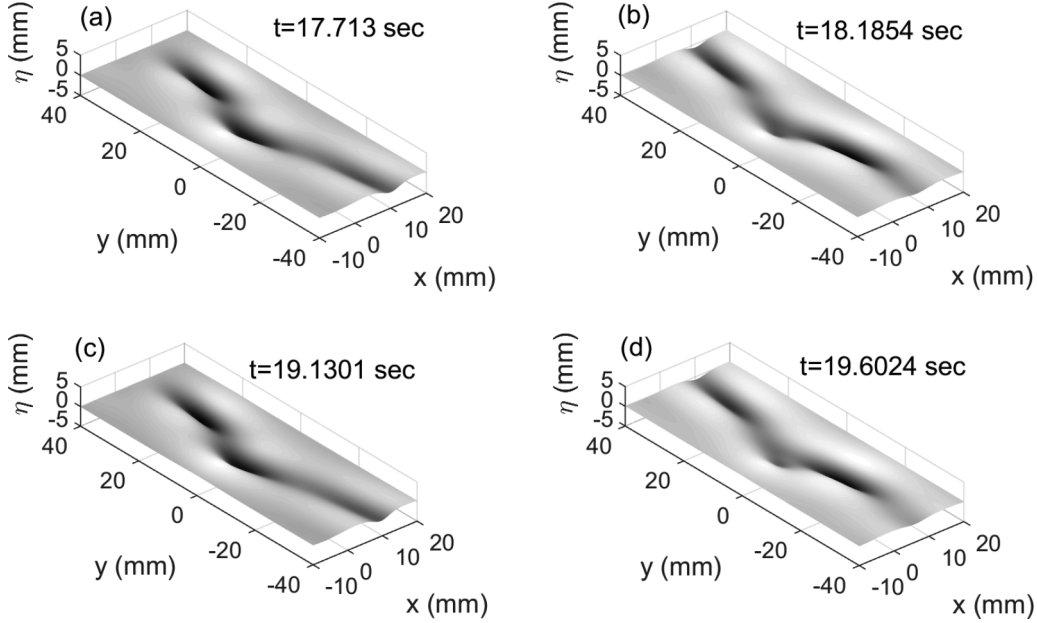
FIG. 5. Irregular asymmetric shedding of 3D local depressions corresponding to Fig. 1(f) ($\alpha = 0.97$, $t = 13 \sim 35$ s). The left moving forcing is located at the origin ($x = 0$, $y = 0$).

shedding period is about 1.3 s. As the forcing speed further increases ($0.99 \leqslant \alpha \leqslant 1$), regular symmetric shedding of 3D local depressions are observed as shown in Fig. 7 ($\alpha = 0.99$), which corresponds to Fig. 1(h). In Fig. 7(a), one can see the obliquely shed 3D local depressions on both sides of the left-moving forcing. At the same time, near the forcing position, the growth of a new 3D local depression is seen that is going to be obliquely shed on both sides of the left-moving forcing. Then, as shown in Figs. 7(b) and 7(c), the shed 3D local depressions gradually disappear due to viscous dissipation while new 3D local depressions are obliquely shed on both sides of the left-moving forcing under the influence of viscous dissipation. Finally, when the forcing speed exceeds 1 ($\alpha > 1$), steady "V"-shaped surface waves are observed behind the moving forcing as shown in Fig. 8, which corresponds to Fig. 1(j).

IV. LINEAR STABILITY ANALYSIS FOR THE ANTISYMMETRIC SHEDDING

In the present transient simulation with a still-water initial condition, no intentional perturbation is given, while there is unavoidable accumulated numerical perturbations during the time-marching process. These accumulated numerical perturbations are believed to play roles as longitudinal and transverse perturbations to the generated 3D gravity-capillary solitary waves. Since the numerically generated solitary waves are steep with finite-amplitude maximum depressions, they are stable to longitudinal perturbations [13,17,20,21]. For a transverse perturbation, however, the stability of gravity-capillary solitary waves will depend on the symmetry of the perturbation. If the perturbation is symmetric, gravity-capillary solitary waves will be stable. If the perturbation is antisymmetric, gravity-capillary solitary waves will become unstable, and, as a result, irregular asymmetric or regular antisymmetric shedding phenomena of 3D local depressions

will be identified behind the moving forcing. To confirm this conjecture, first, we will perform a linear stability analysis based on the forced model equation, Eq. (1), to identify plausible symmetric and antisymmetric perturbations. Then, these perturbations will be added to steady gravity-capillary solitary wave solutions to Eq. (13). The simulation results of Eq. (1) with these initial conditions will reveal that anti-symmetric perturbations are the cause of the irregular asymmetric or regular anti-symmetric shedding of 3D local depressions. The present approach is not mathematically rigorous, but it gives an idea of what is occurring. From the forced model equation, Eq. (1),

$$\eta_t - \tilde{v}(\eta_{xx} + \eta_{yy}) + \left(\alpha - \tfrac{1}{2}\right)\eta_x - \tfrac{1}{4}H\{\eta_{xx} + 2\eta_{yy} - \eta\}$$
$$- \beta(\eta^2)_x = Ap_x. \tag{16}$$

Now, let us assume that, at some point, a perturbation is introduced (say $t = 0^-$) and vanished ($t = 0^+$) in the forcing,

$$p = \begin{cases} \bar{p}(x, y) + p'(x, y)(t = 0) \\ \bar{p}(x, y)(t > 0) \end{cases}; \quad p' \to 0 \text{ as } x, y \to \pm\infty,$$
$$\tag{17}$$

and, as a result, the resultant wave elevation afterwards is decomposed as follows:

$$\eta = \bar{\eta}(x, y) + \eta'(x, y, t); \quad |\eta'/\bar{\eta}| \ll 1,$$
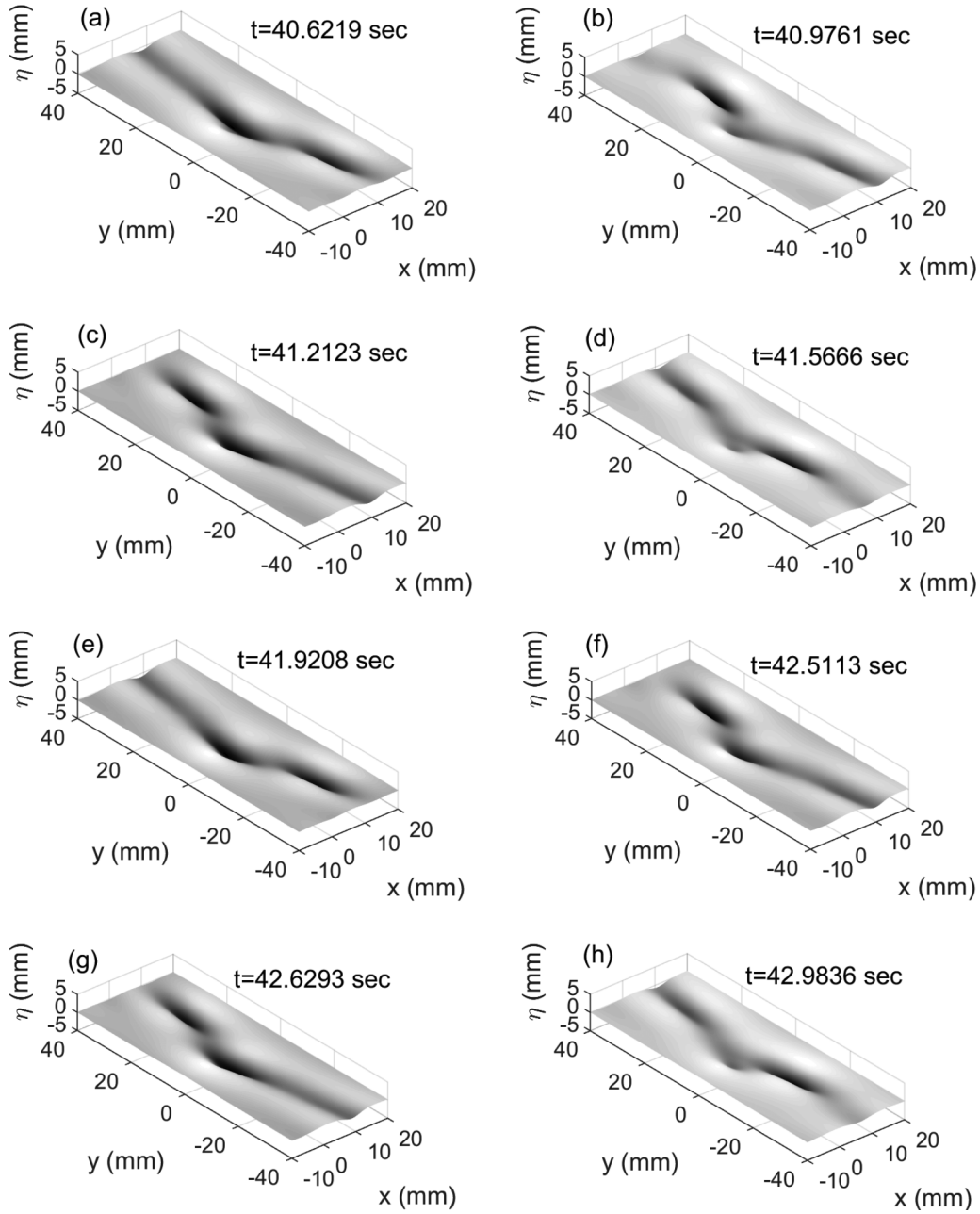$$\eta' \to 0 \quad \text{as } x, y \to \pm\infty, \tag{18}$$

FIG. 6. Regular antisymmetric shedding of 3D local depressions corresponding to Fig. 1(f) ($\alpha = 0.97$, $t > 35$ s). The left-moving forcing is located at the origin ($x = 0$, $y = 0$). Figures 6(a)–6(d) are the same as Figs. 6(e)–6(h), respectively, and the shedding period is about 1.3 s.

where $\bar{p} = \exp(-2x^2 - 2y^2)$, and $\bar{\eta}$ and η' satisfy the following equations, respectively:

$$-\tilde{\nu}(\bar{\eta}_{xx} + \bar{\eta}_{yy}) + \left(\alpha - \frac{1}{2}\right)\bar{\eta}_x - \frac{1}{4}H\{\bar{\eta}_{xx} + 2\bar{\eta}_{yy} - \bar{\eta}\}$$

$$- \beta(\bar{\eta}^2)_x = A\bar{p}_x \quad \text{(Eq. (13))}, \tag{19}$$

$$\eta'_t - \tilde{\nu}(\eta'_{xx} + \eta'_{yy}) + \left(\alpha - \frac{1}{2}\right)\eta'_x - \frac{1}{4}H\{\eta'_{xx} + 2\eta'_{yy} - \eta'\}$$

$$- 2\beta(\bar{\eta}\eta')_x = \begin{cases} A p'_x & (t = 0) \\ 0 & (t > 0) \end{cases}, \tag{20}$$

where $\bar{\eta}$ is the intermediate steady wave solution (for example, Fig. 4 for $\alpha = 0.97$) which is symmetric in y. Now, let us assume the following localized form of the perturbation term η':

$$\eta'(x, y, t) = \varphi(x, y)e^{\lambda t}; \quad \varphi \to 0 \quad \text{as } x, y \to \pm\infty. \tag{21}$$

Then, from Eqs. (20) and (21),

$$\lambda\varphi - \tilde{\nu}(\varphi_{xx} + \varphi_{yy}) + \left(\alpha - \frac{1}{2}\right)\varphi_x - \frac{1}{4}H\{\varphi_{xx} + 2\varphi_{yy} - \varphi\}$$

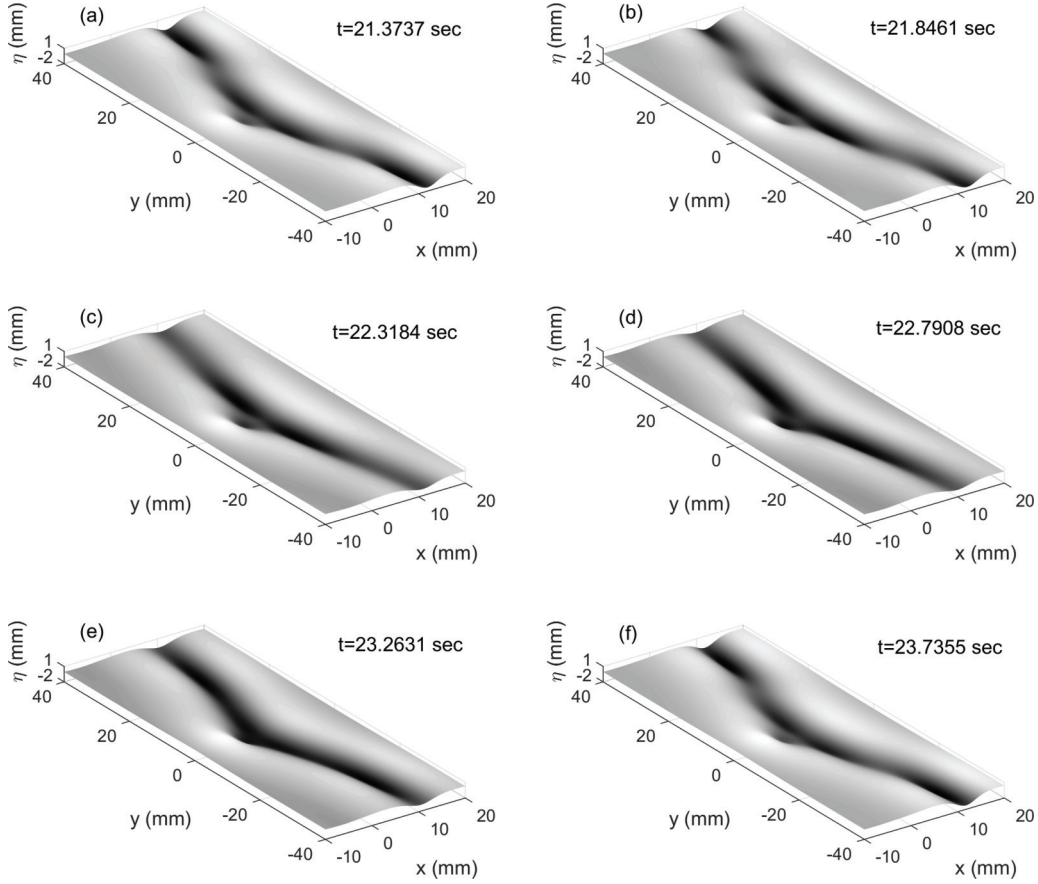$$- 2\beta(\bar{\eta}\varphi)_x = \begin{cases} A p'_x & (t = 0) \\ 0 & (t > 0) \end{cases}. \tag{22}$$

FIG. 7. Regular symmetric shedding of 3D local depressions corresponding to Fig. 1(h) ($\alpha = 0.99$). The left-moving forcing is located at the origin ($x = 0$, $y = 0$).

Upon expanding φ, λ, and p' in the ascending power of $0 < \varepsilon \ll 1$,

$$\varphi = \varphi_0 + \varepsilon\varphi_1 + \varepsilon^2\varphi_2 + \cdots, \tag{23}$$

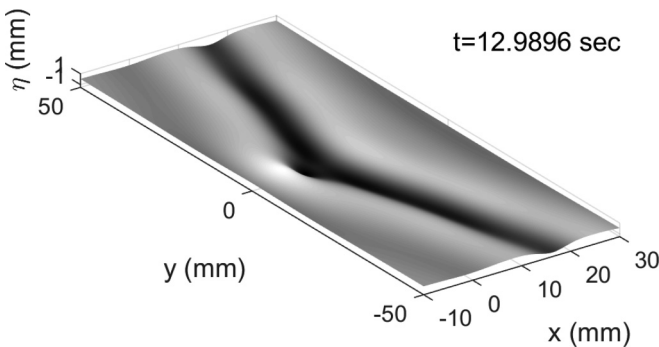$$\lambda = \lambda_0 + \varepsilon\lambda_1 + \varepsilon^2\lambda_2 + \cdots, \tag{24}$$

FIG. 8. Steady wave solution corresponding to Fig. 1(j) ($\alpha = 1.01$). The left-moving forcing is located at the origin ($x = 0$, $y = 0$). Steady "V"-shaped surface waves are formed behind the moving forcing.

$$p' = \begin{cases} \frac{\partial \bar{p}}{\partial x} + \varepsilon \frac{\partial^2 \bar{p}}{\partial x^2} + \cdots \text{ (perturbed in the } x \text{ direction)} \\ \frac{\partial \bar{p}}{\partial y} + \varepsilon \frac{\partial^2 \bar{p}}{\partial y^2} + \cdots \text{ (perturbed in the } y \text{ direction)} \end{cases}, \tag{25}$$

and substituting Eqs. (23)–(25) into Eq. (22), one obtains a series of equations according to the order of magnitude $O(1)$, $O(\varepsilon)$, $\cdots$. At zeroth order $O(1)$,

$$O(1) : L\varphi_0 = -\lambda_0\varphi_0 + \begin{cases} A\bar{p}_{xx} \text{(perturbed in the } x \text{ direction)} \\ A\bar{p}_{xy} \text{(perturbed in the } y \text{ direction)} \end{cases}, \tag{26}$$

where L denotes the following linear operator:

$$L = -\tilde{\nu}\left(\frac{\partial^2}{\partial x^2} + \frac{\partial^2}{\partial x^2}\right) + \left(\alpha - \frac{1}{2}\right)\frac{\partial}{\partial x}$$
$$- \frac{1}{4}H\left\{\frac{\partial^2}{\partial x^2} + 2\frac{\partial^2}{\partial x^2} - 1\right\} - 2\beta\bar{\eta}_x - 2\beta\bar{\eta}\frac{\partial}{\partial x}. \tag{27}$$

A solution to the problem, Eq. (26), is

$$\lambda_0 = 0, \tag{28}$$

$$\varphi_0 = \begin{cases} \bar{\eta}_x & \text{(symmetric in } y) \\ \bar{\eta}_y & \text{(antisymmetric in } y) \end{cases}. \tag{29}$$
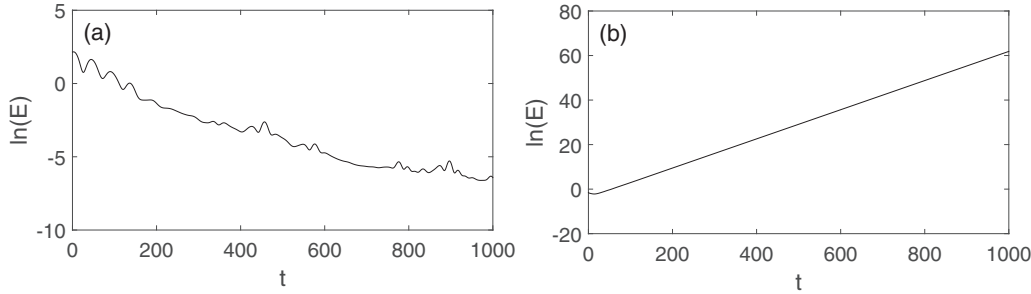
FIG. 9. Time evolution of the energy $E = \int_{-\infty}^{\infty} \int_{-\infty}^{\infty} \eta'^2 dx dy$ (t vs ln E), for the (a) symmetric initial condition $\eta'(x, y, t = 0) = \bar{\eta}_x$ and (b) antisymmetric initial condition $\eta'(x, y, t = 0) = \bar{\eta}_y$.

Proceeding to the next order $O(\varepsilon)$,

$$O(\varepsilon) : L\varphi_1 = -\lambda_0 \varphi_1 - \lambda_1 \varphi_0$$
$$+ \begin{cases} A\bar{p}_{xxx} \text{(perturbed in the } x \text{ direction)} \\ A\bar{p}_{xyy} \text{(perturbed in the } y \text{ direction)} \end{cases}. \quad (30)$$

Appealing to the usual solvability argument, it is possible to assess whether this nonhomogeneous equation has a solution or not. The adjoint operator L^{adj} to the operator L is

$$L^{\text{adj}} = -\tilde{\nu}\left(\frac{\partial^2}{\partial x^2} + \frac{\partial^2}{\partial x^2}\right) + \left(\alpha - \frac{1}{2}\right)\frac{\partial}{\partial x}$$
$$- \frac{1}{4}H\left\{\frac{\partial^2}{\partial x^2} + 2\frac{\partial^2}{\partial y^2} - 1\right\} - 2\beta\bar{\eta}\frac{\partial}{\partial x}. \quad (31)$$

The solution to $L^{\text{adj}}\eta^{\text{adj}} = 0$ is $\eta^{\text{adj}} = 0$(due to existence of the viscous operator) and, thus, Eq. (30) is solvable, which, however, does not provide useful information on the stability. Therefore, instead of proceeding to higher-order analytics, the effect of the leading-order perturbation term [Eq. (29)] on the transverse instability is numerically investigated.

A. Numerical results for the linearized equation of the perturbation η'

Equation (20) will determine the transient behavior of the perturbation η', i.e., growth or decay. For example, for $\alpha = 0.97$, the following two initial conditions [from Eq. (29)] are used in the transient numerical simulations for the symmetric and antisymmetric perturbations, respectively:

$$\eta'(x, y, t = 0) = \bar{\eta}_x, \quad (32)$$

$$\eta'(x, y, t = 0) = \bar{\eta}_y. \quad (33)$$

Figure 9 shows the time evolution of the energy $E = \int_{-\infty}^{\infty} \int_{-\infty}^{\infty} \eta'^2 dx dy$ (t versus ln E), which shows the exponential decay and growth for the symmetric [Fig. 9(a)] and antisymmetric [Fig. 9(b)] cases, respectively.

B. Numerical results for the full nonlinear equation

The model equation, Eq. (1), is solved numerically using two initial conditions; symmetrically and antisymmetrically perturbed steady forced 3D gravity-capillary solitary waves, $\bar{\eta}(x, y; \alpha)$ for $\alpha = 0.97$ [Eq. (13) or (19)]. For a symmetric perturbation, the initial condition is set as follows:

$$\eta(x, y, t = 0) = \bar{\eta} + \bar{\eta}_x. \quad (34)$$

In this case, as expected from the numerical result for the linearized equation of the symmetric perturbation η' [Fig. 9(a)], no shedding is observed [Fig. 10(a)]. Therefore, the steady forced 3D gravity-capillary solitary waves are stable to a symmetric transverse perturbation. For an antisymmetric perturbation,

$$\eta(x, y, t = 0) = \bar{\eta} + \bar{\eta}_y. \quad (35)$$

Figure 10(b) shows irregular asymmetric shedding of 3D local depressions according to time. Compare to the still-water initial condition [Fig. 1(f)], which shows the resultant regular antisymmetric shedding, the present case with a different initial condition, Eq. (35), does not show a regular antisymmetric shedding. Therefore, one can conclude that irregular asymmetric or regular antisymmetric shedding phenomena of 3D local depressions is caused by the onset of transverse instability of forced 3D gravity-capillary solitary
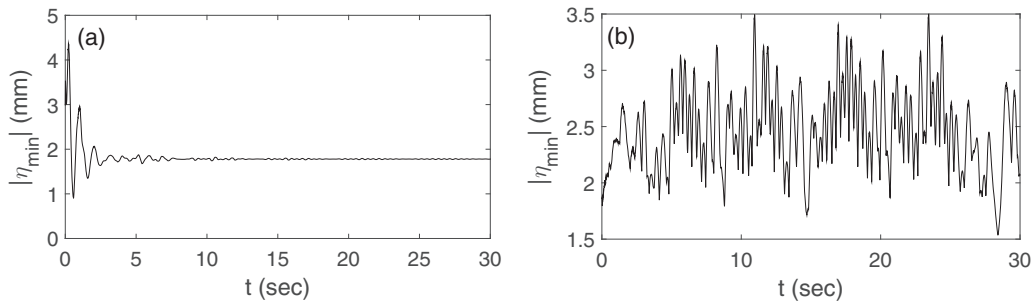

FIG. 10. Time histories of the maximum depressions of the solutions to Eq. (1) for the (a) symmetric initial condition $\eta'(x, y, t = 0) = \bar{\eta} + \bar{\eta}_x$ and (b) antisymmetric initial condition $\eta'(x, y, t = 0) = \bar{\eta} + \bar{\eta}_y$.

waves, which is originated by an antisymmetric perturbation, $\eta' = \bar{\eta}_y$, Eq. (33).

V. SUMMARY

The main theme of the present work is the antisymmetric shedding phenomena of 3D local depressions originated from the transverse instability of steady forced gravity-capillary solitary waves generated by a moving air forcing on the surface of deep water, which are numerically investigated based on a model equation. Although simple relative to the full water wave equation, the usefulness of this model equation was experimentally proved in relevant previous works [16,23–25,28]. Three different states are identified according to forcing speeds U below $c_{\min}$. At relatively low speeds below a certain speed $c_1(U < c_1)$, a steady circular dimple is observed below the moving forcing. At relatively high speeds above a certain speed c_2 $(c_2 < U < c_{\min})$, symmetric shedding phenomena of 3D depressions are observed behind the moving forcing. At intermediate speeds $(c_1 \leqslant U \leqslant c_2)$, after the first transient period, the solution approaches a steady 3D gravity-capillary solitary wave solution. This solitary wave solution maintains its stability for some time, after which an irregular asymmetric shedding of 3D local depressions occurs during the second transient period [26]. Furthermore, when the forcing speed (U) is very close to c_1, after the second transient period of the irregular asymmetric shedding, the final state is an almost regular shedding of 3D local depressions. When the forcing speed (U) is very close to c_2, after the second transient period of the irregular asymmetric shedding, the final state is a regular antisymmetric shedding of 3D local depressions. In the simulation, no intentional perturbation is given, while there is unavoidable accumulated numerical perturbations during the time-marching process. These accumulated numerical perturbations are believed to play roles as longitudinal and transverse perturbations to the generated 3D gravity-capillary solitary waves. These gravity-capillary solitary waves are stable as long as the perturbation is longitudinal. For a transverse perturbation, however, the stability of gravity-capillary solitary waves depends on the symmetry of the perturbation. If the perturbation is symmetric, gravity-capillary solitary waves are stable. If the perturbation is antisymmetric, gravity-capillary solitary waves become unstable, and, as a result, the irregular

asymmetric or regular antisymmetric shedding phenomena of 3D local depressions are identified behind the moving forcing. In addition to these long-time numerical simulations, based on the linear stability analysis, the stability characteristics are investigated analytically and numerically. For a symmetric perturbation, the initial perturbation decays exponentially according to time. For antisymmetric perturbations, the initial perturbation grows exponentially according to time. The behavior of the perturbation is related to the onset of the transverse instability of forced 3D gravity-capillary solitary waves and further explains the resultant irregular asymmetric or regular antisymmetric shedding phenomena of 3D local depressions.

APPENDIX: DERIVATION OF EQ. (1) [16,25,28,29]

From the inviscid dispersion relation of the potential-flow theory for linear sinusoidal gravity-capillary waves on deep water,

$$\omega^2 = g\kappa + \frac{\sigma}{\rho}\kappa^3, \tag{A1}$$

where ω is the angular frequency, g is gravitational acceleration, κ is the magnitude of the wave-number vector $\kappa = \sqrt{k^2 + l^2}$, k is the wave number in the x direction, l is the wave number in the y direction, σ is the coefficient of the surface tension, and ρ is the fluid density. Assuming a linear wave propagating in positive or negative x direction, the phase speed $c = \pm\mathrm{sgn}(k)\omega/\kappa$ features a minimum $c_{\min} = (8\sigma g/\rho)^{1/4}$ at a nonzero finite wave number $(k,l) = (\pm\sqrt{\rho g/\sigma}, 0)$. Using the length scale $L = \sqrt{\sigma/\rho g}$ and the timescale $T = \sqrt{\sigma/\rho g}/c_{\min}$, the dispersion relation, Eq. (A1), becomes dimensionless,

$$\omega^2 = \tfrac{1}{2}(\kappa + \kappa^3), \tag{A2}$$

whose phase-speed minimum becomes $c_{\min} = 1$ at $(k,l) = (k_m, l_m) = (\pm 1, 0)$. To capture the essential wave phenomena near the minimum phase speed $c_{\min}$, Eq. (A2) is Taylor-expended around $(k,l) = (k_m, l_m)$ [13,23,25,29]:

$$
\begin{aligned}
\omega(k, l) &= \pm\mathrm{sgn}(k)\sqrt{\frac{1}{2}(\kappa + \kappa^3)} = \pm\mathrm{sgn}(k)\sqrt{\frac{1}{2}}\sqrt{(k^2 + l^2)^{1/2} + (k^2 + l^2)^{3/2}} \\
&\approx \pm\mathrm{sgn}(k)\Bigg(\omega(k_m, l_m) + \frac{\partial\omega}{\partial k}\bigg|_{(k_m,l_m)}(k - k_m) + \frac{\partial\omega}{\partial l}\bigg|_{(k_m,l_m)}(l - l_m) + \frac{\partial^2\omega}{\partial k^2}\bigg|_{(k_m,l_m)}(k - k_m)^2 \\
&\quad + 2\frac{\partial^2\omega}{\partial k\partial l}\bigg|_{(k_m,l_m)}(k - k_m)(l - l_m) + \frac{\partial^2\omega}{\partial l^2}\bigg|_{(k_m,l_m)}(l - l_m)^2\Bigg) \\
&= \pm\frac{1}{4}\mathrm{sgn}(k)(1 + 2|k| + k^2 + 2l^2).
\end{aligned}
\tag{A3}
$$

Assuming a left-going wave, the linear dispersion relation is

$$\omega = -\tfrac{1}{4}\mathrm{sgn}(k)(1 + 2|k| + k^2 + 2l^2). \tag{A4}$$

The decay of the amplitude of a linear sinusoidal wave on deep water propagating in the x direction was derived by Lamb [30] as follows:

$$A = A(t' = 0) \exp(-2\nu k'^2 t')$$

$$\text{(primed : dimensional quantities)}, \qquad \text{(A5)}$$

where $\nu = 10^{-6} \text{m}^2/\text{s}$ is the kinematic viscosity of water. Using the length scale $L = \sqrt{\sigma/\rho g}$ and the timescale $T = \sqrt{\sigma/\rho g}/c_{\min}$, the decay rate can be expressed as a following dimensionless form:

$$2\nu k'^2 t' = 2\nu \frac{k^2}{L^2}(Tt) = \nu(4g)^{1/4}(\rho/\sigma)^{3/4}k^2 t \equiv \tilde{\nu}_0 k^2 t. \quad \text{(A6)}$$

Therefore, the viscous effect can be reflected in the inviscid dispersion relation as follows:

$$\omega = -\tfrac{1}{4}\text{sgn}(k)(1 + 2|k| + k^2 + 2l^2) - i\tilde{\nu}(k^2 + l^2). \quad \text{(A7)}$$

Here, $\tilde{\nu} = C\nu(4g)^{1/4}(\rho/\sigma)^{3/4} = C\tilde{\nu}_0$ is the dimensionless kinematic viscosity, where $\nu = 10^{-6}\text{m}^2/\text{s}$ is the kinematic viscosity of water, and C is the parameter ($C = 1$ for linear sinusoidal waves, $C > 1$ for nonlinear solitary waves), which determines the decay rate of waves [31]. From Eq. (A7), one can replace variables (ω, k, l) in the temporal and spatial frequency domains with those (t, x, y) in the physical domain:

$$\omega \to -i\frac{\partial}{\partial t}, \quad k \to i\frac{\partial}{\partial x}, \quad l \to i\frac{\partial}{\partial y}, \quad \text{sgn}(k) \to -i\mathcal{H},$$
$$\text{(A8)}$$

where $\mathcal{H}\{f\} = \mathcal{F}^{-1}\{-i\,\text{sgn}(k)\mathcal{F}\{f\}\}$ stands for the Hilbert transform, with

$$\mathcal{F}\{f\} = \int_{-\infty}^{\infty} f(x)e^{-ikx}dx \qquad \text{(A9)}$$

being the Fourier transform. Consequently, one obtains the following model equation for linear viscous gravity-capillary waves on deep water:

$$\eta_t - \tilde{\nu}(\eta_{xx} + \eta_{yy}) - \tfrac{1}{2}\eta_x - \tfrac{1}{4}\mathcal{H}\{\eta_{xx} + 2\eta_{yy} - \eta\} = 0, \quad \text{(A10)}$$

where $\eta = \eta(x, y, t)$ is the wave elevation, and the subscript denotes the partial differentiation. To account for the nonlinearity originated from nonlinear free-surface kinematic and dynamic boundary conditions and the left-moving forcing, one can add a quadratic nonlinearity term $\beta(\eta^2)_x$ and the forcing $Ap(x + \alpha t)$ in the equation:

$$\eta_t - \tilde{\nu}(\eta_{xx} + \eta_{yy}) - \tfrac{1}{2}\eta_x - \beta(\eta^2)_x - \tfrac{1}{4}\mathcal{H}\{\eta_{xx} + 2\eta_{yy} - \eta\}$$
$$= Ap_x(x + \alpha t). \qquad \text{(A11)}$$

By replacing x with $x + \alpha t$ in Eq. (A11), the wave equation, which is expressed in the left-moving reference with a dimensionless speed $\alpha = c/c_{\min}$, is obtained as follows:

$$\eta_t - \tilde{\nu}(\eta_{xx} + \eta_{yy}) + \left(\alpha - \tfrac{1}{2}\right)\eta_x - \beta(\eta^2)_x$$
$$- \tfrac{1}{4}\mathcal{H}\{\eta_{xx} + 2\eta_{yy} - \eta\} = Ap_x(x). \qquad \text{(A12)}$$

To determine the nonlinear coefficient β, one can consider the following inviscid forcing-free model equation from Eq. (A12):

$$\eta_t + \left(\alpha - \tfrac{1}{2}\right)\eta_x - \beta(\eta^2)_x - \tfrac{1}{4}\mathcal{H}\{\eta_{xx} + 2\eta_{yy} - \eta\} = 0.$$
$$\text{(A13)}$$

In the weakly nonlinear small-amplitude limit near $\alpha = 1$, the solution to Eq. (A13) can be expressed as

$$\eta = \tfrac{1}{2}\varepsilon\{S(X, Y, T)e^{ix} + \text{c.c.}\} + \tfrac{1}{2}\varepsilon^2\{S_2(X, Y, T)e^{2ix}$$
$$+ \text{c.c.}\} + \cdots, \qquad \text{(A14)}$$

where $\alpha = 1 - \varepsilon^2 (0 < \varepsilon \ll 1)$, $(X, Y) = \varepsilon(x, y)$, and $T = \varepsilon^2 t$. Substituting Eq. (A14) into Eq. (A13), one obtains the following nonlinear Schrödinger (NLS) equation:

$$iS_T - S + \tfrac{1}{4}S_{XX} + \tfrac{1}{2}S_{YY} + 4\beta^2|S|^2 S = 0. \quad \text{(A15)}$$

However, from the full water-wave or Euler equation on deep water, the NLS equation is derived as [32]

$$iS_T - S + \tfrac{1}{4}S_{XX} + \tfrac{1}{2}S_{YY} + \tfrac{11}{32}|S|^2 S = 0. \quad \text{(A16)}$$

Finally, by equating Eqs. (A15) and (A16), the nonlinear coefficient is determined as $\beta = \sqrt{11/2}/8$.

[1] T. R. Akylas, Phys. Fluids A **5**, 789 (1993).

[2] M. S. Longuet-Higgins, J. Fluid Mech. **252**, 703 (1993).

[3] B. Kim and T. R. Akylas, J. Fluid Mech. **540**, 337 (2005).

[4] E. I. Părău, J.-M. Vanden-Broeck, and M. J. Cooker, J. Fluid Mech. **536**, 99 (2005).

[5] M. D. Groves and S. M. Sun, Arch. Ratio. Mech. Anal. **188**, 1 (2008).

[6] M. S. Longuet-Higgins, J. Fluid Mech. **200**, 451 (1989).

[7] J.-M. Vanden-Broeck and F. Dias, J. Fluid Mech. **240**, 549 (1992).

[8] E. I. Părău, J.-M. Vanden-Broeck, and M. J. Cooker, Phys. Fluids. **19**, 082102 (2007).

[9] P. A. Milewski, Comm. Math. Sci. **3**, 89 (2005).

[10] M. Maleewong, R. Grimshaw, and J. Asavanant, Eur. J. Mech. B/Fluids **24**, 502 (2005).

[11] E. I. Părău, J.-M. Vanden-Broeck, and M. J. Cooker, Phys. Fluids **17**, 122101 (2005).

[12] D. C. Calvo and T. R. Akylas, J. Fluid Mech. **452**, 123 (2002).

[13] B. Akers and P. A. Milewski, Stud. Appl. Math. **122**, 249 (2009).

[14] P. A. Milewski, J.-M. Vanden-Broeck, and Z. Wang, J. Fluid Mech. **664**, 466 (2010).

[15] B. Kim and T. R. Akylas, J. Fluid Mech. **557**, 237 (2006).

[16] B. Park and Y. Cho, J. Fluid Mech. **834**, 92 (2018).

[17] B. Akers and P. A. Milewski, SIAM J. Appl. Math. **70**, 2390 (2010).

[18] B. Kim, J. Eng. Math. **74**, 19 (2012).

[19] Z. Wang and J.-M. Vanden-Broeck, SIAM J. Appl. Math. **75**, 978 (2015).

[20] T. R. Akylas and Y. Cho, Phil. Trans. R. Soc. A **366**, 2761 (2008).

[21] B. Akers and P. A. Milewski, Stud. Appl. Math. **121**, 49 (2008).

[22] X. Zhang, J. Fluid Mech. **289**, 51 (1995).

[23] J. D. Diorio, Y. Cho, J. H. Duncan, and T. R. Akylas, Phys. Rev. Lett. **103**, 214502 (2009).

[24] J. D. Diorio, Y. Cho, J. H. Duncan, and T. R. Akylas, J. Fluid Mech. **672**, 268 (2011).

[25] Y. Cho, J. D. Diorio, T. R. Akylas, and J. H. Duncan, J. Fluid Mech. **672**, 288 (2011).

[26] N. Masnadi and J. H. Duncan, J. Fluid Mech. **810**, 448 (2017).

[27] N. Masnadi and J. H. Duncan, J. Fluid Mech. **814**, R1 (2017).

[28] B. Park and Y. Cho, J. Fluid Mech. **808**, 168 (2016).

[29] Y. Cho, Comput. Fluids **96**, 253 (2014).

[30] H. Lamb, *Hydrodynamics*, 6th ed. (Dover Publications, New York, 1993).

[31] M. S. Longuet-Higgins, J. Fluid Mech. **344**, 271 (1997).

[32] S. J. Hogan, Proc. R. Soc. Lond. A **402**, 359 (1985).